Int. J. Heat Mass Transfer. Vol. 30, No. 11, pp. 2341–2356, 1987
Printed in Great Britain

0017-9310/87 $3.00+0.00

Mass and heat transfer by high Rayleigh number convection in a porous medium heated from below

OSVAIR V. TREVISAN
Faculdade de Engenharia, Universidade Estadual de Campinas, 13100 Campinas SP, Brazil

and

ADRIAN BEJAN
Department of Mechanical Engineering and Materials Science, Duke University,
Durham, NC 27706, U.S.A.

(*Received* 2 *September* 1986 *and in final form* 10 *April* 1987)

Abstract—This paper outlines a combined theoretical and numerical study of the mass transfer effected by high Rayleigh number Bénard convection in a two-dimensional saturated porous layer heated from below. The focus of this study is on the Darcy flow, heat transfer and mass transfer scales of a single cell (roll) that exists in the steady two-dimensional convection regime. The numerical solutions are based on the complete governing equations for two-dimensional flow, and cover the Rayleigh number range 50–2000. The numerical results compare favorably with the theoretical conclusions of a scale analysis that is based on the recognition of (i) two temperature difference scales in the cell, (ii) a flow field without horizontal boundary layers, and (iii) thermal top and bottom end-regions that are not slender enough to be boundary layers. Writing Le for the Lewis number, the overall mass transfer rate or Sherwood number is shown to scale as $Le^{1/2}Ra^{7/8}$ if $Le > Ra^{1/4}$, as $Le^2 Ra^{1/2}$ if $Ra^{-1/4} < Le < Ra^{1/4}$, and as $O(1)$ if $Le < Ra^{-1/4}$. The transition from the Darcy flow to the inertia-dominated Forschheimer flow and the scales of the Forschheimer regime are discussed in the closing section.

1. INTRODUCTION

THE SUBJECT of Bénard convection in a horizontal porous layer has received considerable attention over the past four decades because of its relevance to geophysical fluid dynamics, geothermal reservoir engineering and thermal insulation design. Reviews of the contemporary advances in this domain have been presented by Cheng [1, 2], Nield [3], McKibbin [4] and Bejan [5]. A related phenomenon that has received much less attention is the combined heat and mass transfer driven by both temperature and concentration differences across the porous layer. The study of this phenomenon began with Nield's [6] seminal paper on the onset of convection in a layer where the buoyancy effect is due to temperature and concentration gradients, and continued with more recent analytical studies of the near-critical convection regime [7–11]. In this paper we consider an aspect that so far has not been discussed, namely, the high Rayleigh number regime characterized by heat and mass transfer processes that are strongly dominated by convection.

The present study consists of numerical experiments and a complete scale analysis of the flow, temperature and concentration fields in a two-dimensional porous medium where the buoyancy effect is due entirely to temperature gradients. Our primary objective is to determine the mass transfer potential of the heat-transfer-driven flow. However, since the flow field forms independently of the concentration field, we use this opportunity to re-examine from a purely theoretical standpoint the scaling trends of two-dimensional convection driven by heating from below, and to propose an alternative to the scaling theories advanced by Elder [12], Palm *et al.* [13], Robinson and O'Sullivan [14] and Bejan [15].

2. PHYSICAL MODEL AND PROBLEM STATEMENT

The system selected for analysis is the two-dimensional region occupied by the fluid-saturated porous medium shown in Fig. 1. The fluid is subjected to a destabilizing vertical temperature gradient by maintaining top and bottom boundaries at different temperatures, T_1 and T_0, such that $T_1 > T_0$ in cases where the fluid has the property to expand upon heating at constant pressure ($\beta > 0$). The ensuing flow is driven solely by the buoyancy effect associated with temperature gradients. Transported by this flow is a non-reacting chemical species the concentration C of which is maintained at different levels (C_1, C_0) along the two horizontal boundaries of the porous layer. The focus of the numerical experiments and scale analysis of this study is on the relationship between the temperature field, which drives the flow, and the concentration field that results from the interaction between the flow and the imposed concentration difference $|C_1 - C_0|$.

NOMENCLATURE

b	Forschheimer's constant, equation (50)
c	specific heat of solid
c_P	specific heat at constant pressure
C	concentration
ΔC	overall concentration difference
ΔC_c	core concentration difference, measured horizontally
D	mass diffusivity
Da	Darcy number, K/H^2
g	gravitational acceleration
H	height
K	permeability
L	horizontal dimension of flow domain
Le	Lewis number, α/D
n	number of rolls (cells)
Nu	overall Nusselt number, equation (18)
P	pressure
Pr	Prandtl number, ν/α
Pr_e	effective Prandtl number, $Pr_p Da$
Pr_p	porous medium Prandtl number, equation (53)
Ra	Rayleigh number, equation (12)
Sh	overall Sherwood number, equation (19)
t	time
T	temperature
ΔT	overall temperature difference
ΔT_c	core temperature difference, measured horizontally
u, v	horizontal and vertical velocity components
x, y	horizontal and vertical Cartesian coordinates.

Greek symbols

α	thermal diffusivity
β	coefficient of volumetric thermal expansion
δ_h	thickness of thermal end region
δ_m	thickness of vertical mass stream
δ_u	thickness of horizontal flow along the end wall
δ_v	thickness of vertical plume
μ	viscosity
ν	kinematic viscosity
ρ	density
σ	heat capacity ratio
ϕ	porosity
ψ	stream function.

Other symbols

$(\ )_{avg}$	average
$(\ )_f$	fluid phase
$(\ )_{max}$	maximum
$(\ )_s$	solid phase
$(\hat{\ })$	dimensionless variables, equations (9)–(11).

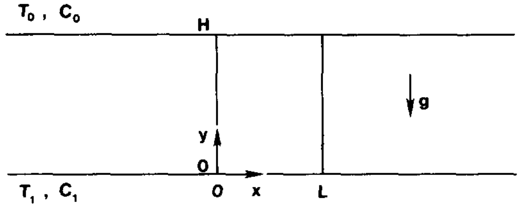

Fig. 1. Schematic of two-dimensional porous layer heated from below and subjected to a concentration difference in the vertical direction.

The flow model consists of the usual incompressible flow assumption coupled with the Boussinesq approximation whereby the density variations are neglected everywhere except in the buoyancy term of the momentum equation. The porous medium is modeled as homogeneous and isotropic, and the volume-averaged flow through the pores is assumed to be slow enough so that it obeys Darcy's law (in other words, the local Reynolds number based on pore diameter and volume-averaged velocity is of $O(1)$ or less). Local thermal equilibrium is assumed between the solid and liquid phases of the medium.

According to the above model, the conservation equations for mass, momentum and energy in two-dimensional flow are [1, 2]

$$\frac{\partial u}{\partial x}+\frac{\partial v}{\partial y}=0 \tag{1}$$

$$\frac{\partial u}{\partial y}-\frac{\partial v}{\partial x}=-\frac{Kg\beta}{\nu}\frac{\partial T}{\partial x} \tag{2}$$

$$\sigma\frac{\partial T}{\partial t}+u\frac{\partial T}{\partial x}+v\frac{\partial T}{\partial y}=\alpha\left(\frac{\partial^2 T}{\partial x^2}+\frac{\partial^2 T}{\partial y^2}\right) \tag{3}$$

where K is the Darcy-flow permeability of the medium. Parameter σ is the heat capacity ratio

$$\sigma=\phi+(1-\phi)\frac{(\rho c)_s}{(\rho c_P)_f} \tag{4}$$

ϕ the porosity, and $(\rho c)_s$ and $(\rho c_P)_f$ the specific heat capacities of solid matrix and fluid mixture, respectively. The rest of the symbols are defined in Fig. 1. According to the same model, the equation that accounts for the conservation of constituent can be written as [15]

$$\phi\frac{\partial C}{\partial t}+u\frac{\partial C}{\partial x}+v\frac{\partial C}{\partial y}=D\left(\frac{\partial^2 C}{\partial x^2}+\frac{\partial^2 C}{\partial y^2}\right) \tag{5}$$

where C is the concentration (expressed as kilograms of constituent per unit volume of porous medium). The coefficient D is the mass diffusivity of the constituent through the solution-saturated porous medium, $D = \phi d$, where d is the mass diffusivity through the solution alone.

Although the object of this study is the steady-state heat and mass transfer across the horizontal layer, the time derivative terms are retained in equations (3) and (5) in order to produce time-dependent solutions that tend to a steady state: this added feature allows us to investigate the oscillatory flows that persist in those cases where steady-state solutions do not exist. In dimensionless form the governing equations read

$$\nabla^2 \hat{\psi} = -\frac{\partial \hat{T}}{\partial \hat{x}} \tag{6}$$

$$\frac{\partial \hat{T}}{\partial \hat{t}} + \frac{\partial \hat{\psi}}{\partial \hat{y}}\frac{\partial \hat{T}}{\partial \hat{x}} - \frac{\partial \hat{\psi}}{\partial \hat{x}}\frac{\partial \hat{T}}{\partial \hat{y}} = \frac{1}{Ra}\nabla^2 \hat{T} \tag{7}$$

$$\frac{\phi}{\sigma}\frac{\partial \hat{C}}{\partial \hat{t}} + \frac{\partial \hat{\psi}}{\partial \hat{y}}\frac{\partial \hat{C}}{\partial \hat{x}} - \frac{\partial \hat{\psi}}{\partial \hat{x}}\frac{\partial \hat{C}}{\partial \hat{y}} = \frac{1}{Ra\,Le}\nabla^2 \hat{C} \tag{8}$$

where $Le = \alpha/D$ and where $(\hat{\ })$ indicates the new dimensionless variables

$$\hat{x} = \frac{x}{H}, \quad \hat{y} = \frac{y}{H}, \quad \hat{\psi} = \frac{\psi}{\alpha\,Ra} \tag{9}$$

$$\hat{T} = \frac{T - T_0}{T_1 - T_0}, \quad \hat{C} = \frac{C - C_0}{C_1 - C_0} \tag{10}$$

$$\hat{t} = \frac{\alpha\,Ra}{H^2 \sigma} t. \tag{11}$$

The streamfunction ψ is defined in the usual way, $u = \partial\psi/\partial y, v = -\partial\psi/\partial x$, and the Darcy modified Rayleigh number is based on the temperature difference and the vertical dimension

$$Ra = \frac{Kg\beta(T_1 - T_0)H}{\alpha\nu}. \tag{12}$$

The dimensionless form of the boundary conditions sketched in Fig. 1 is

$$\hat{\psi} = 0, \quad \hat{T} = 0, \quad \hat{C} = 0 \quad \text{at } \hat{y} = 1 \tag{13}$$

$$\hat{\psi} = 0, \quad \hat{T} = 1, \quad \hat{C} = 1 \quad \text{at } \hat{y} = 0. \tag{14}$$

The domain of the numerical analysis is a rectangular region of horizontal length L. The boundary conditions invoked along the vertical sides are those of impermeability, zero heat transfer and zero mass transfer (see, e.g. Blake *et al.* [16])

$$\hat{\psi} = 0, \quad \frac{\partial \hat{T}}{\partial \hat{x}} = 0, \quad \frac{\partial \hat{C}}{\partial \hat{x}} = 0 \quad \text{at } \hat{x} = 0, L/H. \tag{15}$$

3. NUMERICAL METHOD

Numerical solutions were developed for the transient problem in which a temperature difference is imposed suddenly across the porous medium. The governing equations were discretized based on the control volume formulation described by Patankar [17]. The power law scheme was used in order to evaluate the heat flux and the mass flux across the boundaries of each control volume. The time derivatives were discretized in accordance with the fully implicit scheme.

The initial condition consisted of setting $\hat{\psi} = 0$ and $\hat{T} = 0$ throughout the domain, and the flow was initiated by changing the bottom wall temperature to $\hat{T} = 1$. The $\hat{\psi}$, $\hat{T}$ and $\hat{C}$ fields that form after a time interval $\Delta\hat{t}$ were sought based on the point-by-point iterative method: this method was used repeatedly until the changes in $\hat{\psi}$, $\hat{T}$ and $\hat{C}$ between two successive iterations satisfied the convergence criterion

$$\frac{\sum_{ij} |\tau_{ij}^{l+1} - \tau_{ij}^{l}|}{\sum_{ij} |\tau_{ij}^{l}|} < 10^{-5} \tag{16}$$

where (i, j) are the grid numbers and l is the number of iterations. The solution obtained in this manner was used as the initial guess in the search for the solution that prevails at the end of the next time interval. The evolution in time of the flow, temperature and concentration fields was documented in terms of solutions at discrete time intervals $\Delta\hat{t}$. Special numerical accuracy tests indicated that the size of the time interval $\Delta\hat{t}$ has no effect on the flow, heat and mass transfer solution that prevails at a certain time $\hat{t}$.

The convergence to a final steady-state solution was decided by comparing the overall heat and mass transfer rates evaluated along the top and bottom boundaries. In all the steady-state solutions discussed in the present study the absolute value of the error parameter

$$\text{Err} = \frac{(Nu, Sh)_{\hat{y}=1} - (Nu, Sh)_{\hat{y}=0}}{(Nu, Sh)_{\hat{y}=1} + (Nu, Sh)_{\hat{y}=0}} \tag{17}$$

was less than 1%. The overall Nusselt and Sherwood numbers are both defined with reference to the respective pure diffusion rates

$$Nu = -\int_0^{L/H} \left(\frac{\partial \hat{T}}{\partial \hat{y}}\right)_{\hat{y}=0,1} \mathrm{d}\hat{x} \tag{18}$$

$$Sh = -\int_0^{L/H} \left(\frac{\partial \hat{C}}{\partial \hat{y}}\right)_{\hat{y}=0,1} \mathrm{d}\hat{x}. \tag{19}$$

The two-dimensional domain of Fig. 1 was covered with an array of $(m-2) \times (p-2)$ square control volumes. The four boundaries were represented by control volumes of zero thickness. The effect of grid spacing or number of control volumes is illustrated in Table 1, where m and p represent the total number of control volumes in the vertical and horizontal directions, respectively. As expected, the numerical accuracy and the time needed for convergence increase as the number of control volumes increases. A satisfactory tradeoff between accuracy and computation cost was achieved by always placing 20 control volumes in the direction that corresponds to the shorter of the two sides of the domain (i.e. $m = 20$ if $H/L < 1$, and

Table 1. The sensitivity of the numerical solution to the fineness of the grid ($Ra = 200$, $H/L = 2$, $Le = 1$)

Grid fineness $m \times p$	Nu, Sh	Number of CPUs
22×12	4.08	131
30×16	4.06	412
38×20	4.04	1022
46×24	4.04	2321

Table 2. Numerical results showing the effect of Rayleigh number and geometric aspect ratio on the overall heat and mass transfer rates ($Le = 1$)

Ra	$m \times p$	H/L	Nu, Sh	n
50	34×22	1.60	1.00	1
	26×20	1.33	1.26	1
	23×20	1.17	1.37	1
	28×26	1.08	1.40	1
	22×22	1.00	1.42	1
	28×30	0.93	1.40	1
	21×24	0.86	1.37	1
100	48×20	3.00	1.02	1
	38×20	2.00	2.09	1
	32×20	1.67	2.46	1
	28×20	1.44	2.62	1
	29×22	1.35	2.65	1
	27×22	1.25	2.68	1
	36×30	1.21	1.53	2
	22×20	1.11	1.76	2
	22×22	1.00	2.09	2
	22×26	0.83	2.46	2
	20×28	0.69	2.64	2
200	65×20	3.50	2.25	1
	56×20	3.00	3.10	1
	47×20	2.50	3.79	1
	42×20	2.22	3.96	1
	40×20	2.11	4.02	1
	38×20	2.00	4.04	1
	36×20	1.89	4.05	1
	34×22	1.60	2.71	2
	17×32	0.50	4.09	4
400	42×20	5.00	3.27	1
	74×22	3.60	5.95	1
	59×20	3.17	6.23	1
	56×20	3.00	6.26	1
	53×20	2.83	6.26	1
	42×20	2.22	4.36	2
	38×20	2.00	5.40	2
1000	146×20	8.00	5.86	1
	128×20	7.00	8.69	1
	119×20	6.50	9.62	1
	110×20	6.00	10.41	1
	107×20	5.83	10.62	1
	102×20	5.56	10.84	1
	92×20	5.00	11.08	1
	83×20	4.50	11.01	1
2000	182×20	10.00	13.34	1
	164×20	9.00	15.37	1
	146×20	8.00	16.54	1
	137×20	7.50	16.82	1
	128×20	7.00	16.91	1

$p = 20$ if $H/L > 1$; Table 2). The number of control volumes along the longer side of the domain was chosen such that $(m-2)/(p-2)$ always equalled the geometric aspect ratio H/L.

Underrelaxation was used in order to accelerate the convergence of the solution. Values of the relaxation parameter were 0.7 for the $\hat{\psi}$ and $\hat{T}$ fields, and the range 0.8–1 for the $\hat{C}$ field in the case of large Lewis numbers (i.e. relatively thin concentration boundary layers). In many cases the $H \times L$ domain was narrow enough to house a unicellular flow: given the rough symmetry of the single cell about the vertical mid-plane, the bottom-to-top, horizontal ends-to-middle marching scheme presented a better convergence performance relative to the traditional left-corner-up-and-right scheme.

4. RESULTS

There are two sides to the combined heat and mass transfer phenomenon addressed in this study, a classical part, which is relatively well understood, and a newer part that served as the chief motivation for this work. The classical aspect concerns the Bénard-type flow driven by heating from below in a shallow porous layer. It has been established that in the steady-state convective regime that exists at Rayleigh numbers immediately above critical, the flow consists of cells (rolls) the number and slenderness of which depend on the Rayleigh number. The cells become more slender and multiply as the Rayleigh number increases. Even in numerical studies conducted in two-dimensional domains of finite horizontal extent, the cells exhibit a 'natural' horizontal length scale that—if shorter than L—governs the process of discrete multiplication of the cells as Ra increases.

It is also known that the thermal convection pattern exhibits a transition from steady to time-dependent (simply-periodic) flow as the Rayleigh number increases above approximately 400. The transition and the unsteady state were first documented experimentally by Combarnous and LeFur [18], Caltagirone *et al.* [19] and Combarnous and Bories [20], and via numerical simulations by Horne and O'Sullivan [21] and Caltagirone [22]. A very recent numerical study of two-dimensional time-dependent convection in a square porous domain concluded that the transition to simply-periodic convection occurs at $Ra \simeq 390$ [23]. For this reason, the two-dimensional steady-state solutions developed in the present study refer physically to the convection regime that occurs at Rayleigh numbers lower than 400, that is, in the Ra/Ra_c range 1–10, where Ra_c is the critical Rayleigh number ($4\pi^2$). However, we determined two-dimensional steady-state solutions for Rayleigh numbers as high as 2000, by executing the numerical calculations in sufficiently narrow and tall domains that house only one cell (steady-state solutions persist in the Ra range 400–2000 due to the flow-straightening effect played by the slender vertical region, $H/L \gg 1$). We did this in

Table 3. The effect of the Lewis number on the overall mass transfer rate (the numbers listed in this table represent the values of *Sh*; the corresponding *Nu* values are listed in line with $Le = 1$)

	Ra, (H/L)				
Le	50 (1.00)	100 (1.25)	200 (2.00)	400 (3.00)	1000 (5.83)
0.02					1.01
0.04					1.04
0.1			1.09	1.16	1.24
0.2	1.02	1.15	1.32	1.58	1.87
0.4	1.08	1.50	2.01	2.79	3.87
1	1.42	2.68	4.06	6.26	10.62
2	2.12	4.04	6.17	9.83	18.32
4	3.19	5.84	8.93	14.47	27.84
10	5.19	9.55	14.71	24.03	46.29
20	7.49	13.73	21.52	32.76	
40	10.62	18.50	30.11		
100	14.71				

order to determine with greater accuracy the Rayleigh number dependence of the various flow, heat transfer and mass transfer scales that are revealed by the solutions. This higher degree of accuracy is needed in order to see the 'trends' and test the results of the scale analysis of Section 5, which is based on a two-dimensional steady-state cellular flow model (Fig. 9).

An additional incentive for extending the calculations to $Ra = 2000$ was the wish to verify Robinson and O'Sullivan's [14] numerical results for the same range, which were based directly on the steady-state version of the governing equations. It is worth noting that the physical occurrence of the two-dimensional flow structure described in this and other numerical studies [13, 14] has been demonstrated in Hele–Shaw cell experiments by Elder [12].

The numerical experiments described in this paper are not intended to suggest in any way that at such high *Ra* values the actual flow in an unbounded horizontal layer is steady and two-dimensional.

The present numerical solutions fall into two categories, experiments designed to verify the dependence of cell slenderness on Rayleigh number, Table 2, and experiments designed to document the effect of Rayleigh and Lewis numbers on the overall Sherwood number, Table 3. In the first set of experiments, the Rayleigh number was assigned a value in the range 50–2000 and, with *Ra* fixed, the aspect ratio H/L was decreased from one run to the next. Physically, a sequence of such experiments would take place in a layer with fixed height (H) and bottom–top temperature difference ($T_1 - T_0$), where the horizontal dimension of the medium (L) increases steadily. As the $H \times L$ domain is widened, the flow progresses towards the convective regime and, consequently, the overall Nusselt number and the cell flow rate increase.

The relationship between *Nu* and L/H at constant *Ra* is shown in Fig. 2. One interesting aspect of this relation is the maximum approached by *Nu* as the domain becomes increasingly wider: beyond this maximum the number of cells doubles suddenly and the overall Nusselt number drops sharply. In Fig. 2 this effect is illustrated only for $Ra = 100$, however, it is found at other Rayleigh numbers as well (Table 2). Furthermore, the cell doubling phenomenon repeats itself as the domain becomes wider, as shown by the $Ra = 200$ runs summarized in Table 2.

It is worth noting that the first continuous portion of the Nu–H/L curve in Fig. 2 (i.e. the single-cell portion) agrees very well with the data published earlier by Caltagirone [22]. In particular, the aspect ratio that corresponds to the maximum *Nu* in single-cell flow is practically the same as in Caltagirone's study. One difference that we found is that the flow approaches a steady state over the second continuous portion of the Nu–H/L curve (after cell doubling), in other words, contrary to Caltagirone's conclusions, the present long-time solutions were not characterized by persistent fluctuations. Relevant to this comparison is the fact that the numerical solutions converged smoothly for all the values of *Ra* as long as the number of cells remained constant. However, the solution behaved differently in the case of the critical L/H values associated with cell doubling: in Fig. 2 this range corresponds to the gap between the smooth portions of the Nu–L/H curve. In these narrow domains the numerical solution did not converge, in fact, even the transient solution was accurate only during a short time interval immediately after $\hat{t} = 0$. The developing streamline pattern showed that the solution becomes unstable as it fluctuates between the original flow and one with twice as many cells. The original flow resides in the upper portion of the porous medium, while the splitting of the cells takes place in the lower portion. On either side of the narrow cell-doubling range of L/H values the transient solution proceeded smoothly and stably towards an unambiguous (unique, reproducible) steady state: two examples of this smooth evolution are given in Fig. 3.

The overall Nusselt number results of Table 2 are presented in Fig. 4 as a plot of *Nu* vs $H/(L/n)$, where n is the number of cells observed in each steady-state solution. The use of the cell geometric aspect ratio $H/(L/n)$ on the abscissa is intentional: its purpose is to show that the Nusselt number depends primarily on the geometry of the constituent cells, in other words, that the shift from Fig. 2 to Fig. 4 allows all the *Nu* data for a single *Ra* to fall practically on a single curve.

A representative set of streamlines, isotherms and constant concentration lines is presented in Figs. 5(a)–(d). The case is one where the overall Nusselt number has reached a maximum as H/L decreased at constant *Ra* (Table 2), in other words, the counterclockwise single-cell pattern of Fig. 5(a) illustrates the natural height/thickness ratio that corresponds to $Ra = 200$. The isotherms of Fig. 5(b) show that the top and bottom ends of the cell are characterized by intense vertical temperature gradients. Furthermore, the ver-

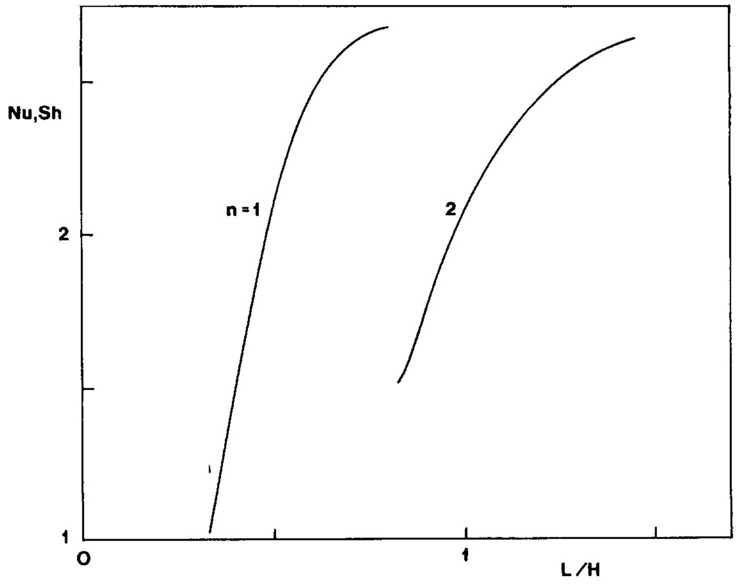

FIG 2. The effect of the geometric aspect ratio (L/H) on the overall Nusselt number (Nu) while holding the Rayleigh number fixed ($Ra = 100$).

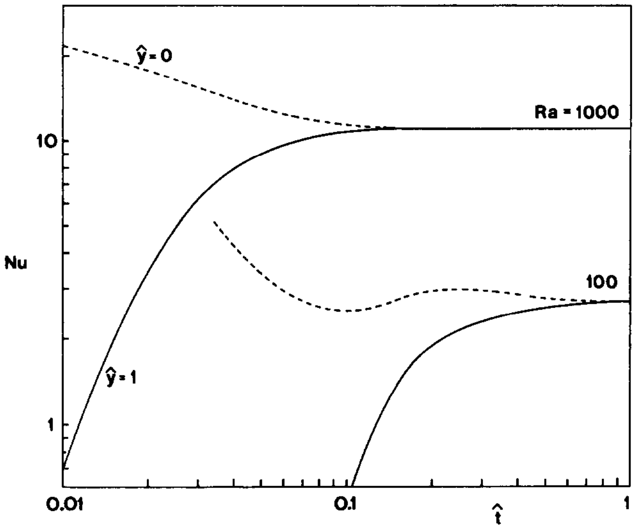

FIG. 3. The smooth evolution of the heat transfer solution to a steady state, and the Ra effect on the duration of the time-dependent solution.

tical segments of the circulation loop are two slender plumes: note that although the plumes are insulated along their outer boundaries, they do exchange heat all along their height, which is of order H (the observation that the two plumes function like a long counterflow heat exchanger is essential to being able to predict analytically the scales of the flow, temperature and concentration fields (Section 5)).

Figure 5(b) is also a plot of the constant concentration lines that are calculated when $Le = 1$. Examined together with Figs. 5(c) and (d), these plots show how the top and bottom concentration boundary layers become thinner as the Lewis number assumes progressively larger values. At the same time we note that the thickness of the concentration plumes that line the vertical sides of the cell decreases, i.e. that the direct mass transfer between the two branches of the vertical counterflow diminishes. At $Le = 20$, for example, the 'core' of the cell is practically in a state of uniform concentration.

The effect of the Lewis number on the overall Sherwood number is documented through the solutions summarized in Table 3. These solutions are for (Ra, H/L) pairs that yield maximum or near-maximum Nusselt numbers in the manner illustrated in Fig. 4. The Sherwood numbers assembled in Table 3 increase with both Ra and Le: Fig. 6 shows that in the high Lewis number limit the Sherwood number increases as $Le^{1/2}$, and that in the vicinity of $Le \sim 1$ the $Sh(Le)$ curve is considerably steeper. To explain these trends theoretically is the preliminary objective of the scale analysis presented in the next section.

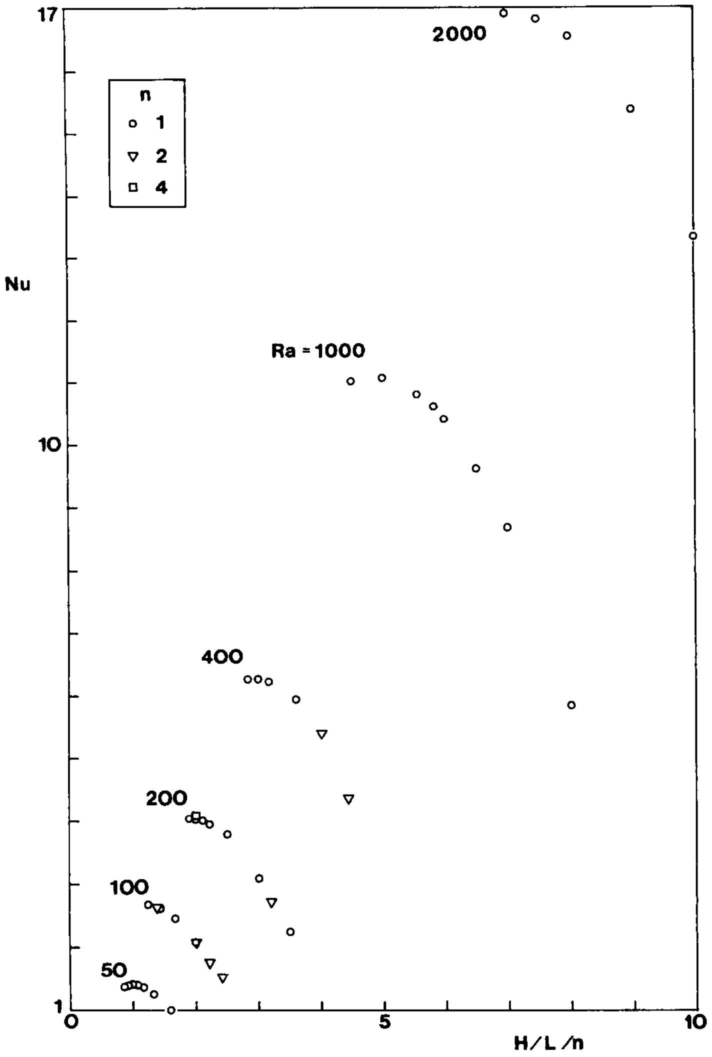

FIG. 4. The dependence of the overall Nusselt number on the Rayleigh number and the height/thickness ratio of an individual cell, $H/(L/n)$.

5. SCALE ANALYSIS

The scaling trends exhibited by two-dimensional cellular convection in a porous layer heated from below have attracted considerable attention. Table 4 outlines a summary of the main results of the scale analyses that have been proposed so far in connection with the flow/heat transfer part of the phenomenon addressed in this paper. The scales of the mass transfer part of the phenomenon are intimately related to those addressed by the studies mentioned in Table 4: for this reason, an understanding of mass transfer trends requires first an understanding of the flow and heat transfer scales.

5.1. *Flow and heat transfer*

The scaling results of Elder [12], Palm *et al.* [13], Robinson and O'Sullivan [14] and Bejan [15] are listed chronologically in Table 4 in order to highlight the lack of agreement that continues to divide the theoretical domain of the field. Elder's analysis focused only on the thermal boundary layers that line the top and bottom walls of each cell. Bejan's analysis is essentially the same as Elder's, and is presented as one example in a case-by-case coverage of the subject of convection based on scale analysis. Palm *et al.*'s analysis includes a study of the scales of the slender core region between the top and bottom walls. The main difference between Palm *et al.*'s predictions and those of the other theories is the ability to anticipate the $Nu \sim Ra^{1/2}$ scaling law for heat transfer: as shown by the present results (Fig. 7), a scaling law $Nu \sim Ra^{P}$ in which $P < 1$ would fit the data more closely than $Nu \sim Ra$.

Worthy of special mention is Robinson and O'Sullivan's [14] study, in which analyses of both horizontal and vertical boundary layer regions are combined with the empirical adoption of $Nu \sim Ra^{2/3}$ and

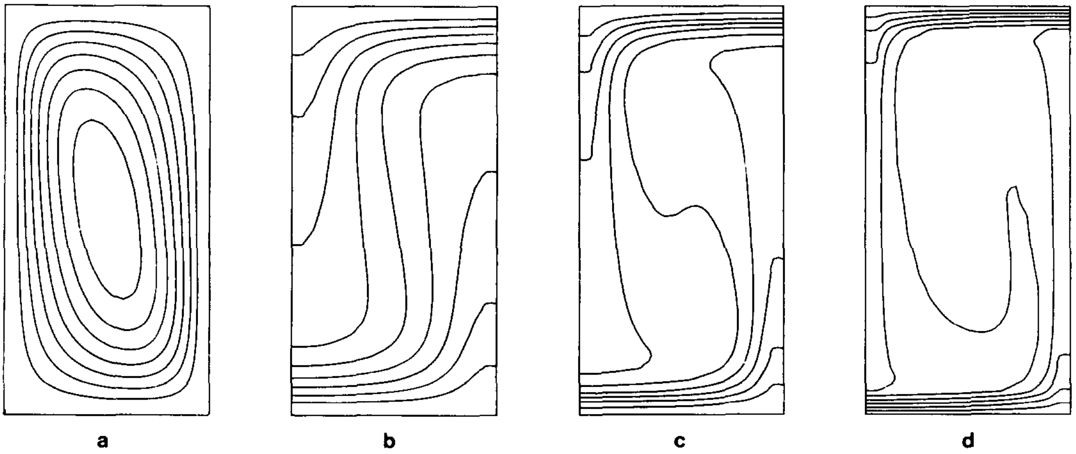

FIG. 5. Numerical solution for $Ra = 200$ and $H/L = 1.89$: (a) streamlines, $\hat{\psi}_{\max} = 0.0313$, $\hat{\psi}_{\min} = 0$, $\Delta\hat{\psi} = 0.004$; (b) isotherms, also constant-concentration lines for $Le = 1$; (c) lines of constant concentration for $Le = 4$; (d) lines of constant concentration for $Le = 20$.

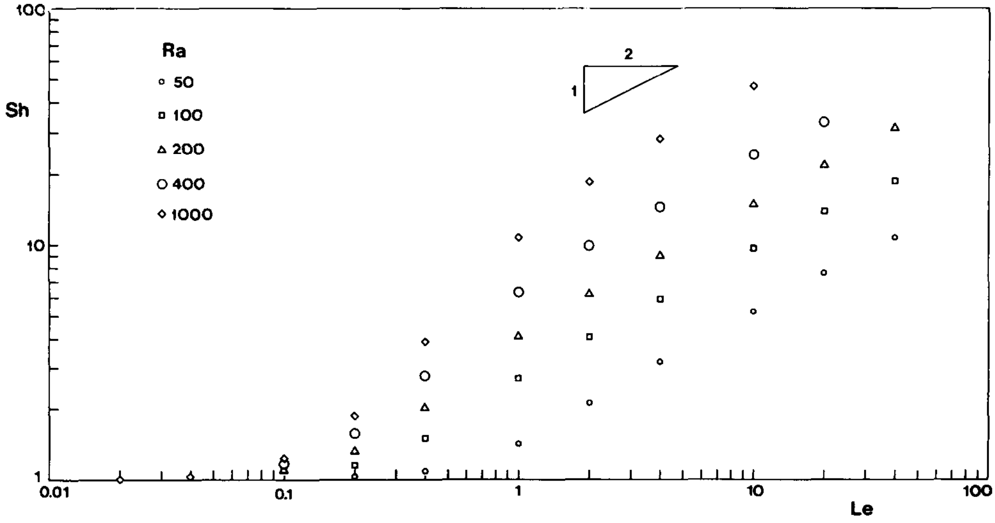

FIG. 6. The Lewis number effect on the overall Sherwood number.

$H/L \sim Ra^{2/3}$ as the correct scaling trends that prevail in the Rayleigh number range 100–2000. These scaling laws were obtained by curve-fitting the numerical Nu and H/L data yielded by Nusselt number maximization experiments similar to the ones conducted in the present study (Fig. 4). Because of their reliance on empirical information, the Robinson and O'Sullivan method goes a long way towards expressing correctly all the flow and heat transfer scales of the phenomenon.

Obviously, the problem of anticipating these scales from a purely theoretical point of view is still open to discussion. We used the present experiments and the ultimate objective of discovering the scaling-correct correlation for mass transfer results, as an opportunity to shed new light on the scales of the flow and heat transfer problem. Stimulated by Robinson and O'Sullivan [14] and conversations with Professor O'Sullivan [24] we examined closely the Rayleigh number dependence of certain quantities that can be calculated along the periphery of each $H \times L$ cell at the stage where the overall Nu reaches its maximum. The results of these calculations are listed in Table 5, where $\hat{u}_{\mathrm{avg}}$ is the horizontal velocity averaged along the top (or bottom) horizontal wall, $\hat{v}_{\mathrm{avg}}$ is the vertical velocity averaged along the left (or right) vertical boundary, and $\Delta\hat{T}_{\mathrm{c}}$ is the temperature difference measured in the horizontal direction between the two vertical boundaries of the cell $[\hat{T}(L/H, \hat{y}) - \hat{T}(0, \hat{y})]$ and averaged from $\hat{y} = 0$ to 1.

Recalling that the Rayleigh number was used in the nondimensionalization of the flow field, equation (9),

Table 4. Summary of scale analyses of the flow and heat transfer in a two-dimensional porous medium heated from below

Study	Nu	H/L	$v/(\alpha/H)$	$u/(\alpha/H)$	L/δ_h	$\Delta\hat{T}_c$
Elder [12]	Ra		Ra			
Palm *et al.* [13]	$Ra^{1/2}$	$Ra^{1/2}$	Ra		Ra^0	
Robinson and O'Sullivan [14]	$(Ra^{2/3})_*$	$(Ra^{2/3})_*$	$Ra^{5/6}$	$Ra^{2/3}$	Ra^0	$Ra^{-1/6}$
Bejan [15]	Ra	$Ra^{1/2}$	Ra		$Ra^{1/2}$	
Present results, equations (38) and (39)	$Ra^{1/2}$	$Ra^{1/2}$	$Ra^{3/4}$	$Ra^{1/4}$	Ra^0	$Ra^{-1/4}$

$(\ )_*$ = scaling law suggested by an empirical correlation of numerical data.

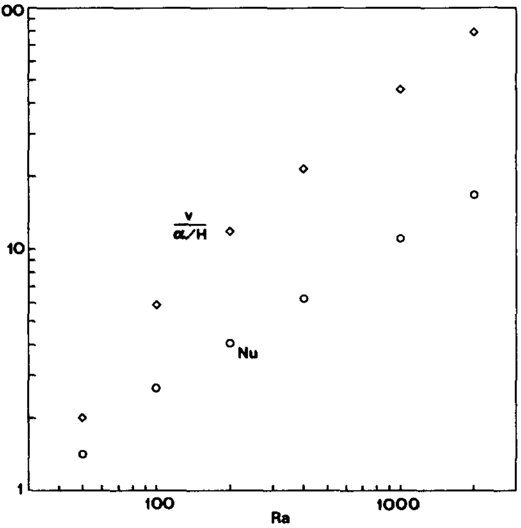

FIG. 7. The effect of Rayleigh number on the overall Nusselt number and the vertical velocity scale.

the complete effect of Ra on the horizontal and velocity scales is brought to light by plotting not $\hat{u}_{avg}$ and $\hat{v}_{avg}$, but

$$\frac{u}{\alpha/H} \sim Ra\,\hat{u}_{avg} \tag{20}$$

$$\frac{v}{\alpha/H} \sim Ra\frac{\hat{\psi}_{max}}{L/H} \tag{21}$$

or

$$\frac{v}{\alpha/H} \sim Ra\,\hat{v}_{avg}. \tag{22}$$

The dimensionless vertical velocity scale $v/(\alpha/H)$ shown in Fig. 7 was calculated with equation (21) based on the $\hat{\psi}_{max}$ and H/L data gathered in Table 5.

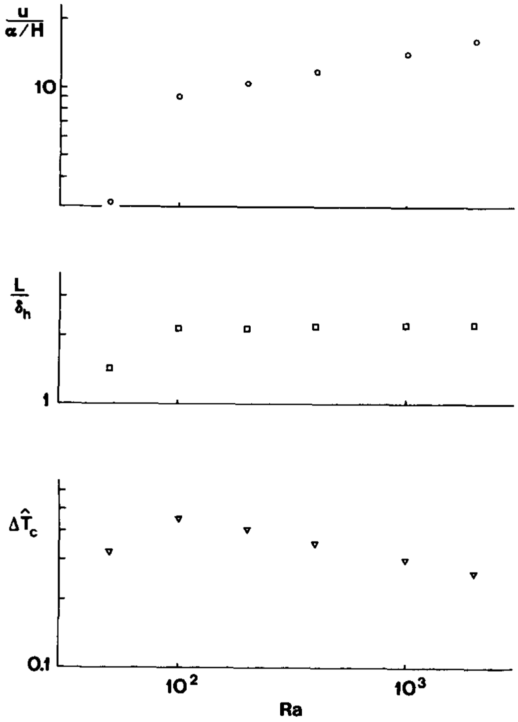

FIG. 8. The effect of Rayleigh number on the horizontal velocity scale (top graph), thermal end region thickness (middle graph) and side-to-side temperature difference (bottom graph).

The horizontal velocity scale $u/(\alpha/H)$ was calculated from equation (20) and Table 5 and plotted as the first graph of Fig. 8. The trends revealed by the data of Figs. 7 and 8 are discussed later in this section.

The first step in the scale analysis of the cellular flow is the identification of certain flow regions that possess certain properties (e.g. slenderness) that dis-

Table 5. Peripheral and overall flow and heat transfer quantities in a single cell that maximizes Nu

Ra	H/L (Nu_{max})	$\hat{\psi}_{max}$	$\hat{u}_{avg}$	$\hat{v}_{avg}$	$\Delta\hat{T}_c$	δ_u/H
50	1.00 (1.42)	0.0396	0.0814	0.0791	0.326	0.486
100	1.25 (2.68)	0.0471	0.0916	0.132	0.453	0.514
200	1.89 (4.05)	0.0313	0.0524	0.148	0.405	0.597
400	2.83 (6.26)	0.0189	0.0297	0.142	0.354	0.636
1000	5.00 (11.08)	0.00912	0.0141	0.131	0.299	0.647
2000	7.5 (16.82)	0.00531	0.0081	0.118	0.263	0.656

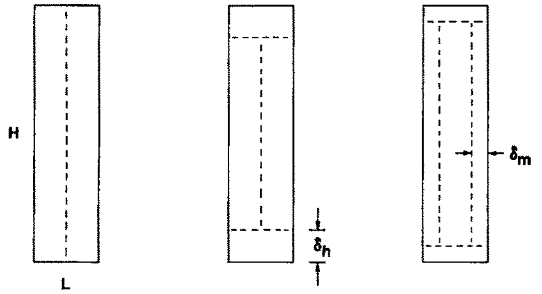

FIG. 9. The structure of the $H \times L$ cell that maximizes *Nu* when *Ra* is fixed: left, flow; middle, temperature; right, concentration ($Le > Ra^{1/4}$).

tinguish them from the remaining regions. Consider the $H \times L$ domain sketched in Fig. 9, and recall that it is 'tall' especially at large Rayleigh numbers (Table 5). The top and bottom walls come in contact with thermal end regions of length L and thermal thickness δ_h, where δ_h is assumed much smaller than H (i.e. $Nu \gg 1$). In a flow region that is sandwiched between the two $L \times \delta_h$ end regions, we recognize the presence of the vertical plume counterflow discussed already in connection with Fig. 5.

One crucial question to consider at this stage is whether the thickness of each vertical plume is of order L or it has a different scale δ_v, where $\delta_v < L$. If the plume thickness scales as L, then the 'core' region of the cell is filled entirely by the plume counterflow (this is the case sketched in Fig. 9). If, on the other hand, the plume thickness scale δ_v is smaller than L, then the counterflowing plumes trap between them a relatively stagnant region the horizontal length scale of which is L. The assumed δ_v scale is calculated from Table 5 by first writing

$$\hat{v}_{\text{avg}} \sim \frac{\partial \hat{\psi}}{\partial \hat{x}} \sim \frac{\hat{\psi}_{\max}}{\delta_v / H} \tag{23}$$

which yields

$$\frac{H}{\delta_v} \sim \frac{\hat{v}_{\text{avg}}}{\hat{\psi}_{\max}}. \tag{24}$$

The H/δ_v values are shown in Fig. 10 next to the H/L ratios that resulted from the *Nu* maximization experiments. The assumed δ_v scale is consistently half the size of L in the *Ra* range 50–2000, in other words, the core is filled completely by the plume counterflow. The comparison presented in Fig. 10 is another indication that the L dimension of the cell that maximizes the overall heat transfer rate is a 'natural' length scale of the flow: the cell chooses a thickness L that leaves room only for the vertical plume counterflow that is exchanged by the two end regions.

Another important observation is that the cellular flow possesses two temperature difference scales, the bottom–top difference $\Delta T = T_1 - T_0$, and the difference measured in the horizontal direction (the difference across the counterflow) ΔT_c, where $\Delta T_c \leqslant \Delta T$.

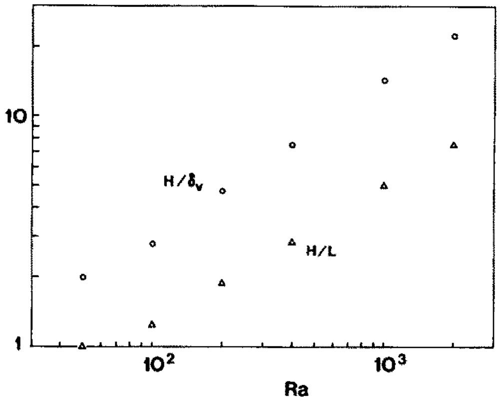

FIG. 10. The *Ra* dependence of H/L and H/δ_v, showing that the vertical plume thickness δ_v scales as L.

We consider first the vertical counterflow region, the vertical and horizontal dimensions of which are of order H and L, and assume that this region is slender, $H \gg L$. The momentum equation (2) requires the following equivalence of scales:

$$\frac{v}{L} \sim \frac{Kg\beta}{\nu} \frac{\Delta T_c}{L}. \tag{25}$$

The energy equation (3) requires

$$v \frac{\Delta T - \Delta T_c}{H} \sim \alpha \frac{\Delta T_c}{L^2} \tag{26}$$

meaning that the heat transfer in the horizontal direction (between the counterflowing plumes) is balanced by the enthalpy picked up or released by each stream as it travels a distance H.

From the mass conservation equation (1) we derive an equation for the horizontal entrainment velocity scale u

$$\frac{u}{L} \sim \frac{v}{H}. \tag{27}$$

Equation (27) implies that the vertical plume flow rate vL turns and proceeds horizontally as a counterflow of velocity u and cross-section H. In other words, the velocity thickness of the horizontal flow is of order H ($H/2$, more accurately), and even along the top and bottom walls the horizontal velocity scale is dictated by the entrainment/detrainment exchange between the vertical plumes. This type of horizontal velocity scaling rules out the existence of distinct velocity boundary layer regions along the top and bottom walls of the porous medium. Note that the same type of horizontal velocity distribution (i.e. one that is spread over the entire height H) is present in Weber's [25] solution for the boundary layer regime in a rectangular porous medium heated from the side.

Although the (u, v) circulation fills the entire $H \times L$ region, a fraction of the vL flow rate turns around through the thermal end regions of size $L \times \delta_h$. The thermal end regions constitute the energy link between the heat transferred through the horizontal boundaries ($y = 0, H$) and the enthalpy carried vertically by the plume counterflow. In each thermal end region the heat transfer problem is one of 'forced convection', in the sense that the flow that sweeps the horizontal wall (the u scale) is dictated by the requirement of mass conservation in the $H \times L$ region. If we assume that the thermal end region is slender

$$\delta_h \ll L \tag{28}$$

then the energy equation (3) requires

$$\frac{\delta_h}{L} \sim \left(\frac{uL}{\alpha}\right)^{-1/2}. \tag{29}$$

The scale analysis that was omitted between equations (28) and (29) is the same as the analysis presented on page 357 in Bejan [15]. Finally, the balance between the wall heat transfer to the end region ($k L \Delta T/\delta_h$) and the enthalpy current associated with the vertical plumes ($\rho v L c_P \Delta T_c$) requires

$$\alpha \frac{\Delta T}{\delta_h} \sim \Delta T_c. \tag{30}$$

Equations (25)–(27), (29) and (30) are sufficient for determining the five unknown scales of the flow/heat transfer problem (u, v, L, δ_h, ΔT_c). If we neglect ΔT_c on the left-hand side of equation (26), i.e. if we assume

$$\Delta T \gg \Delta T_c \tag{31}$$

then we obtain the following scales:

$$\begin{aligned} \frac{u}{\alpha/H} &\sim Ra^{1/6} \\ \frac{v}{\alpha/H} &\sim Ra^{2/3} \\ \frac{L}{H} &\sim Ra^{-1/2} \\ \frac{\delta_h}{H} &\sim Ra^{-1/3} \\ \Delta \hat{T}_c &\sim Ra^{-1/3}. \end{aligned} \tag{32}$$

The Nusselt number is of the order of H/δ_h, therefore an additional result of the analysis is

$$Nu \sim Ra^{1/3}. \tag{33}$$

We assess the merits of this theory by noting first that the $Ra^{1/6}$ dependence of the horizontal velocity scale is supported by the numerical data plotted in the top graph of Fig. 8. Furthermore, the predicted $Ra^{1/6}$ scaling represents a definite improvement over Robinson and O'Sullivan's semi-empirical $Ra^{2/3}$ trend, Table 4. Also interesting is the fact that Robinson and O'Sullivan's $Ra^{2/3}$ scaling agrees well with their own numerical calculations of wall horizontal velocity (those calculations were made at one point along the wall, $x = L/2$, i.e. unlike the present $\hat{u}_{\text{avg}}$ values, which are averaged over the entire length of the wall).

Next, the $Ra^{2/3}$ dependence predicted for the vertical velocity comes close to the trend exhibited by the data in Fig. 7, although the data fall on a power-law curve $\sim Ra^p$, the exponent p of which is slightly greater than 2/3. This experimental trend is supported by Robinson and O'Sullivan's semi-empirical analysis, which yielded an $Ra^{5/6}$ dependence for $v/(\alpha/H)$.

Good agreement is also found between the predicted $Ra^{1/2}$ for H/L and the numerical trend presented in Fig. 10. This prediction agrees also with the results of two previous analyses (Table 4).

The $Ra^{1/3}$ scaling predicted for the overall Nusselt number underestimates the steepness of the numerical Nu line in Fig. 7, which would be fitted better by Palm *et al.*'s $Nu \sim Ra^{1/2}$ or Robinson and O'Sullivan's $Nu \sim Ra^{2/3}$. This particular discrepancy stimulated the improved analysis that concludes with equations (38) later in this section.

Finally, we record the $Ra^{-1/3}$ dependence predicted for the side-to-side temperature difference $\Delta \hat{T}_c$. This is the first instance in which the downward trend exhibited by the $\Delta \hat{T}_c$ data in Fig. 8 is anticipated on a purely theoretical basis. The numerical $\Delta \hat{T}_c$ values, however, decrease less rapidly than $Ra^{-1/3}$ as Ra increases.

The contribution of the preceding theory is that it accounts at least qualitatively for all the scaling trends revealed by numerical experiments. The quantitative mismatch between theory and experiments with regard to the Ra dependence of Nu and $\Delta \hat{T}_c$ invites another look at the basic assumptions of the theory. To begin with, the decrease of $\Delta \hat{T}_c$ with increasing Ra validates the use of equation (31) as an assumption that applies in the high Rayleigh number limit.

Second, the assumption that the fluid inventory of the plume counterflow returns as a horizontal counterflow of transversal length scale H must be tested against numerical experiments. Let δ_u be the transversal length scale of the horizontal flow, where δ_u is not necessarily of order H. We determine the δ_u scale by first writing

$$\hat{u}_{\text{avg}} \sim \frac{\partial \hat{\psi}}{\partial \hat{y}} \sim \frac{\hat{\psi}_{\max}}{\delta_u/H} \tag{34}$$

and then using Table 5 to evaluate

$$\frac{\delta_u}{H} \sim \frac{\hat{\psi}_{\max}}{\hat{u}_{\text{avg}}}. \tag{35}$$

The results of this calculation are listed in the last column of Table 5, and show that in the Ra range of this study δ_u is consistently of order H. This validates the assumption discussed immediately after equation (27).

Third, the scaling results (32) imply that the slenderness ratio of the thermal end regions must vary as

$$\frac{L}{\delta_h} \sim Ra^{-1/6}. \tag{36}$$

The prediction that L/δ_h is a weak function of Ra is supported by the data plotted in Fig. 8, however, equation (36) and the data cast doubt on the assumption that the thermal end region is slender, equation (28). The slenderness ratio appears to be of the order of 2 (i.e. not much greater than one), suggesting that the thermal end region is not a 'boundary layer region'. In this case the effect of longitudinal diffusion ($\alpha \Delta T/L^2$) is no longer negligible relative to transversal diffusion ($\alpha \Delta T/\delta_h^2$) on the right-hand side of the energy equation (3). Consequently, as a way of improving the theory that yielded equations (32), in place of the convection scaling law (29), we use the diffusion balance $\alpha \Delta T/L^2 \sim \alpha \Delta T/\delta_h^2$, which yields

$$\delta_h \sim L. \tag{37}$$

Equations (25)–(27), (30) and (37) are the five scaling laws of the modified theory in which the thermal end region is not assumed to be of the boundary layer type. The scaling results of this alternative theory are

$$\begin{aligned} \frac{u}{\alpha/H} &\sim Ra^{1/4} \\ \frac{v}{\alpha/H} &\sim Ra^{3/4} \\ \frac{L}{H} &\sim Ra^{-1/2} \\ \frac{\delta_h}{H} &\sim Ra^{-1/2} \\ \Delta \hat{T}_c &\sim Ra^{-1/4} \end{aligned} \tag{38}$$

with the additional result for overall Nusselt number

$$Nu \sim Ra^{1/2}. \tag{39}$$

Comparing equation (38) with the first theory, equations (32), and with the data plotted in Figs. 7, 8 and 10, we find that the latest theory anticipates very well all the trends exhibited by the numerical results. The scaling laws (38) are entered at the bottom of Table 4, as our contribution to the twenty year old debate.

The relative success of the present contribution, equations (38) and (39), is due to three decisions that are absent in most if not all the preceding theories, namely,

(i) the recognition of two temperature difference scales, ΔT and ΔT_c;

(ii) the assumption of a flow field without horizontal boundary layers;

(iii) the assumption of thermal end regions that are not slender enough to be boundary layers.

The preliminary version of this theory, equations (32), is based only on assumptions (i) and (ii) and predicts qualitatively all the observed trends. Assumption (iii) has the effect of fine-tuning the eventual solution, equations (38).

5.2. *Mass transfer*

The scaling properties of the overall mass transfer rate can be discussed now with reference to the last drawing of Fig. 9. Let δ_m be the thickness of the mass stream that rides along the centerline of each vertical plume, and assume first that

$$\delta_m < L. \tag{40}$$

In this case the two vertical mass streams do not come in direct contact, since they are separated by an L-thick core of average concentration $\Delta C/2$. The vertical counterflow of the two mass streams carries convectively a constituent mass flow rate of the order of $v\delta_m \Delta C$. The diffusion-referenced Sherwood number is then

$$Sh \sim \frac{v\delta_m \Delta C}{DL\Delta C/H} \tag{41}$$

where the v and L scales are given by equations (38). The problem reduces to finding the mass stream thickness δ_m.

Assuming that the mass stream is slender, $\delta_m \ll H$, the constituent conservation equation (5) expresses a balance between lateral mass diffusion ($D\Delta C/\delta_m^2$) and the amount of constituent absorbed by the clean fluid entrained by the mass stream ($u_m \Delta C/\delta_m$). The entrainment velocity scale u_m is a scale of the $H \times \delta_m$ region; mass conservation in the $H \times \delta_m$ region requires $u_m/\delta_m \sim v/H$ or via equation (27), $u_m/\delta_m \sim u/L$. The constituent conservation scaling law required by equation (5) is therefore

$$\frac{u}{L} \sim \frac{D}{\delta_m^2} \tag{42}$$

which, combined with equations (38) and (41), translates into

$$\delta_m \sim H\, Le^{-1/2}\, Ra^{-3/8} \tag{43}$$

$$Sh \sim Le^{1/2}\, Ra^{7/8}. \tag{44}$$

These results are valid as long as $\delta_m < L$, i.e. when

$$Le > Ra^{1/4}. \tag{45}$$

If the Lewis number is less than $Ra^{1/4}$ the mass stream thickness is of the order of L, and the two mass streams engage in mass exchange over their entire height H. The concentration of each stream varies with y, as the mass lost by one stream is gained by the other. The mass flow rate of the constituent via the vertical counterflow is now $vL\Delta C_c$, where the new scale ΔC_c is the concentration difference measured in the horizontal direction (ΔC_c is analogous to the ΔT_c scale used in the analysis of the flow part of the problem). The stream-to-stream concentration difference ΔC_c is obtained by invoking equation (5) in the $H \times L$ region. The balance between stream-to-stream mass diffusion and longitudinal mass gain

$$v\frac{\Delta C}{H} \sim D\frac{\Delta C_c}{L^2} \tag{46}$$

yields the ΔC_c scale. Relying again on the flow and heat transfer scales (38), we conclude that in this second regime the Sherwood number must scale differently

$$Sh \sim Le^2\, Ra^{1/2}. \tag{47}$$

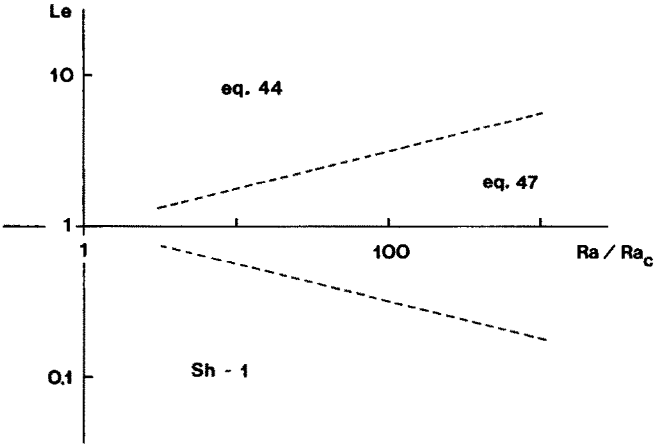

FIG. 11. The *Ra–Le* domain and the four mass transfer regimes possible in two-dimensional convection driven by heat transfer (Ra_c is the critical Rayleigh number, $4\pi^2$).

By intersecting equations (44) and (47) we confirm that equation (47) applies when *Le* is less than $Ra^{1/4}$, i.e. when equation (45) fails. The Sherwood number of equation (47) decreases rapidly as *Le* decreases, however, this trend must end when the mass diffusivity has become so large that the overall mass transfer rate is dictated by diffusion ($Sh \sim 1$). In this way we conclude that equation (47) holds in the *Le* range

$$Ra^{-1/4} < Le < Ra^{1/4} \tag{48}$$

and that *Sh* is of the order of one in the limit of extremely low Lewis numbers, $Le < Ra^{-1/4}$.

Figure 11 summarizes the mass transfer regimes that are possible in two-dimensional natural convection driven by heating from below in a porous medium. The *Ra–Le* field is divided by equation (48) and $Ra \sim Ra_{\text{critical}}$ into four domains: proceeding clockwise, the four mass transfer regimes can be termed 'no flow' ($Sh = 1$), 'high *Le*' (equation (44)), 'intermediate *Le*' (equation (47)) and 'low *Le*' ($Sh \sim 1$).

The numerical data of Table 3 support the Sherwood number scales determined above very well. Earlier in this paper we saw that at high Lewis numbers the Sherwood number increases as $Le^{1/2}$, Fig. 6. The *Ra* dependence of the Sherwood number in the high *Le* limit is similar to the $Ra^{7/8}$ proportionality anticipated in equation (44): e.g. the *Sh* ($Le = 10$) values of Table 3 increase as $Ra^{0.71}$.

The intermediate Lewis number regime, equation (47), explains finally the steeper slope that develops in the *Sh*(*Le*) curve in the vicinity of $Le \sim 1$. The slope becomes increasingly steeper as *Ra* increases, i.e. as the flow travels deeper into the wedge-shaped intermediate *Le* domain of Fig. 11. The *Sh*(*Le*) curve at high (constant) *Ra* has three distinct portions: note that the width of the inner portion (the intermediate *Le* regime) increases as *Ra* increases, in accordance with criterion (48).

6. CONCLUDING REMARKS: THE TRANSITION FROM DARCY FLOW TO FORSCHHEIMER FLOW

The objective of this study was to determine the mass transfer characteristics of two-dimensional Bénard convection through a fluid saturated porous medium. The scale analysis of the single-cell flow and the numerical results obtained in the *Ra* range 50–2000 suggest that the overall mass transfer rate obeys three distinct scaling laws, namely

$$Sh \sim Le^{1/2} Ra^{7/8}, \quad \text{when } Le > Ra^{1/4} \tag{49a}$$

$$Sh \sim Le^2 Ra^{1/2}, \quad \text{when } Ra^{-1/4} < Le < Ra^{1/4} \tag{49b}$$

$$Sh \sim O(1), \quad \text{when } Le < Ra^{-1/4}. \tag{49c}$$

The high-*Le* and low-*Le* behavior (the first and third scaling laws above) is supported conclusively by the overall mass transfer results yielded by numerical experiments. The data obtained in the intermediate Lewis number range $Ra^{-1/4} < Le < Ra^{1/4}$ shows that the Lewis number exponent l in the $Sh \sim Le^l Ra^r$ relation increases steadily as *Ra* increases. Whether the l exponent becomes eventually equal to 2 could, conceivably, be determined by extending the present series of experiments to Rayleigh numbers higher than 2000.

The most important conclusion of this study is that the *Sh*(*Le*, *Ra*) dependence separates into *three* distinct regimes. From an engineering standpoint, this means that numerical Sherwood number results such as those of Fig. 6 cannot be correlated in the usual fashion, i.e. by simply intersecting the two extreme asymptotes (49a) and (49c).

One limitation of the work described here is the assumption that the Darcy flow prevails throughout the 'high Rayleigh number' range that was considered. Under special circumstances that are presented below, it is possible that above a certain Rayleigh number the velocity is sufficiently large to cause the breakdown of the Darcy flow model. The model that captures the transition from Darcy flow to a flow where the fluid inertia is important is the so-called Darcy–Forschheimer model [5], according to which the vectorial momentum equation reads

$$\mathbf{v}+\frac{bK}{\nu}|\mathbf{v}|\mathbf{v}=\frac{K}{\mu}(-\nabla P+\rho\mathbf{g}). \qquad (50)$$

The Darcy-flow momentum equation that was used throughout this study, equation (2), corresponds to setting $b = 0$ on the left-hand side of equation (50). At sufficiently high values of $|\mathbf{v}|$ the second term dominates the left-hand side of equation (50): we shall refer to this flow regime as the Forschheimer flow regime.

The scales of Bénard convection heat transfer in the Forschheimer regime were studied recently by Bejan [5, 26, 27]. The same regime had been documented numerically by Georgiadis and Catton [28] and, experimentally, by Jonsson and Catton [29]. The Georgiadis and Catton work is based on the even more general Darcy–Forschheimer–Brinkman model in which in addition to the Darcy flow resistance and the fluid inertia one accounts also for the no-slip condition along the solid wall of the enclosure. Using a scale analysis analogous to the one that for the Darcy regime yielded $Nu \sim Ra$ [15] (see also Table 4), Bejan showed that above a certain Rayleigh number (i.e. in the Forschheimer regime)

$$Ra > Pr_p \qquad (51)$$

the Nusselt number increases less steeply with the Rayleigh number

$$Nu \sim (Ra\,Pr_p)^{1/2}. \qquad (52)$$

The new group is the 'porous medium Prandtl number' [5, 26, 27] defined as

$$Pr_p = Pr\frac{H}{bK} \qquad (53)$$

where $Pr = \nu/\alpha$. In conclusion, the Darcy-flow conclusions hold if the order of magnitude of Ra does not exceed that of Pr_p.

The present scaling results for the Darcy-flow regime, equations (38) and (39), are based on a Bénard cell model that is more sophisticated than in the early analysis of ref. [15] (review assumptions (i)–(iii) in Section 5). In particular, it is assumed that the cell has two temperature scales, ΔT and ΔT_c. Repeating the scale analysis that led to equations (38) and assuming this time 'Forschheimer flow' instead of Darcy flow, we obtain instead of equations (25), (26), (37) and (30) in order

$$v \sim \left(\frac{g\beta\Delta T}{b}\right)^{1/2} \qquad (54)$$

$$\frac{\Delta T_c}{\Delta T} \sim \frac{vL^2}{\alpha H} \qquad (55)$$

$$\delta_h \sim L \qquad (56)$$

$$\frac{\Delta T_c}{\Delta T} \sim \frac{\alpha}{vL}. \qquad (57)$$

These equations can readily be solved for δ_h to prove that the Nusselt number scaling law for the Forschheimer regime is

$$Nu \sim \frac{H}{\delta_h} \sim (Ra\,Pr_p)^{1/3}. \qquad (58)$$

This scaling law replaces the Darcy-flow law (39) as Ra increases, therefore the transition from Darcy flow to Forschheimer flow occurs when

$$Ra > Pr_p^2. \qquad (59)$$

In conclusion, the flow, heat and mass transfer scales reported between equations (38) and (49) are valid if the order of Ra does not exceed the order of magnitude of Pr_p^2. Note finally that contrary to statements made in refs. [26, 27] the porous medium Prandtl number Pr_p is not the same as Jonsson and Catton's [29] effective Prandtl number Pr_e. The relation between the two is $Pr_p = Pr_e/Da$, where $Da = K/H^2$.

The numerical part of this study can also be extended, e.g. by using equation (50) instead of equation (2). An even more effective step would be to include also the Brinkman term as done by Georgiadis and Catton [28]. Another worthwhile extension would be to relax the 'tall enclosure' assumption, which for most of this study constrained the flow to the single-cell geometry. Relevant to the work of using a wider L/H domain for each flow regime is a recent study communicated by Prasad and Kulacki [30].

Acknowledgements—The numerical part of this study was executed in the Department of Mechanical Engineering of the University of Colorado, Boulder, during Professor Trevisan's term as Visiting Scholar, 1984–1985. Professor Trevisan gratefully acknowledges the hospitality of the Colorado faculty, and the support received from his home institution, the University of Campinas, Brazil. Professor Bejan's work was supported by the National Science Foundation Grant No. MEA-8421250 and by Duke University.

REFERENCES

1. P. Cheng, Heat transfer in geothermal systems, *Adv. Heat Transfer* **14,** 1–105 (1978).
2. P. Cheng, Geothermal heat transfer. In *Handbook of Heat Transfer* (Edited by W. M. Rohsenow, J. P. Hartnett and E. Ganic), 2nd Edn. McGraw-Hill, New York (1985).
3. D. A. Nield, Recent research on convection in a saturated porous medium, *Convective Flows in Porous Media,* Proceedings of a seminar organized by DSIR and CSIRO Institute of Physical Sciences, Wairakei, New Zealand, 3–4 May 1984 (Edited by R. A. Wooding and I. White). DSIR Science Information Publishing Centre, P.O. Box 9741, Wellington (1985).
4. R. McKibbin, Thermal convection in layered and anisotropic porous media: a review, *Convective Flows in Porous Media,* Proceedings of a seminar organized by DSIR and CSIRO Institute of Physical Sciences, Wairakei, New Zealand, 3–4 May 1984 (Edited by R. A. Wooding and I. White). DSIR Science Information Pub-

lishing Centre, P.O. Box 9741, Wellington (1985).

5. A. Bejan, Convective heat transfer in porous media. In *Handbook of Single-phase Convective Heat Transfer* (Edited by S. Kakac, R. K. Shah and W. Aung), Chap. 16. Wiley, New York (1987).
6. D. A. Nield, Onset of thermohaline convection in a porous medium, *Water Resour. Res.* **4,** 553–560 (1968).
7. H. Rubin, Effect of nonlinear stabilizing salinity profiles on thermal convection in a porous medium layer, *Water Resour. Res.* **9,** 211–221 (1973).
8. H. Rubin, Onset of thermohaline convection in a cavernous aquifer, *Water Resour. Res.* **12,** 141–147 (1976).
9. H. Rubin and C. Roth, Instability of horizontal thermohaline flow in a porous medium layer, *Israel J. Tech.* **16,** 216–222 (1978).
10. P. R. Patil and N. Rudraiah, Linear convective stability and thermal diffusion of a horizontal quiescent layer of a two component fluid in a porous medium, *Int. J. Engng Sci.* **18,** 1055–1059 (1980).
11. N. Rudraiah, P. K. Srimani and R. Friedrich, Finite amplitude convection in a two component fluid saturated porous layer, *Int. J. Heat Mass Transfer* **25,** 715–722 (1982).
12. J. W. Elder, Steady free convection in a porous medium heated from below, *J. Fluid Mech.* **27,** 29–48 (1967).
13. E. Palm, J. E. Weber and O. Kvernvold, On steady convection in a porous medium, *J. Fluid Mech.* **54,** 153–161 (1972).
14. J. L. Robinson and M. J. O'Sullivan, A boundary-layer model of flow in a porous medium at high Rayleigh number, *J. Fluid Mech.* **75,** 459–467 (1976).
15. A. Bejan, *Convection Heat Transfer*, Chap. 10. Wiley, New York (1984).
16. K. R. Blake, A. Bejan and D. Poulikakos, Natural convection near 4°C in a water saturated porous layer heated from below, *Int. J. Heat Mass Transfer* **27,** 2355–2364 (1984).
17. S. V. Patankar, *Numerical Heat Transfer and Fluid Flow*. Hemisphere, Washington, D.C. (1980).
18. M. Combarnous et B. LeFur, Transfert de chaleur par convection naturelle dans une couche poreuse horizontale, *C. R. Acad. Sci. Paris* **269B,** 1009–1012 (1969).
19. J. P. Caltagirone, M. Cloupeau et M. Combarnous, Convection naturelle fluctuate dans une couche poreuse horizontale, *C. R. Acad. Sci. Paris* **273B,** 883–836 (1971).
20. M. A. Combarnous and S. A. Bories, Hydrothermal convection in saturated porous media, *Adv. Hydrosci.* **10,** 231–307 (1975).
21. R. N. Horne and J. M. O'Sullivan, Oscillatory convection in a porous medium, *J. Fluid Mech.* **66,** 339–352 (1974).
22. J. P. Caltagirone, Thermoconvective instabilities in a horizontal porous layer, *J. Fluid Mech.* **72,** 269–287 (1975).
23. S. Kimura, G. Schubert and J. M. Straus, Route to chaos in porous medium thermal convection, *J. Fluid Mech.* **166,** 305–324 (1986).
24. M. J. O'Sullivan, Private communication to A. Bejan during the 6th New Zealand Geothermal Workshop, University of Auckland, Geothermal Institute, 7–9 November (1984).
25. J. E. Weber, The boundary layer regime for convection in a vertical porous layer, *Int. J. Heat Mass Transfer* **18,** 569–573 (1975).
26. A. Bejan, The basic scales of natural convection heat and mass transfer in fluids and fluid-saturated porous media, *Int. Commun. Heat Mass Transfer* **14,** 107–123 (1987).
27. A. Bejan, Stressing the "free" in free convection research: the basic scales of heat and mass transfer in fluids and fluid-saturated porous media, Keynote address, *Proceedings of the 1987 ASME–JSME Thermal Engineering Joint Conference* (Edited by P. J. Marto and I. Tanasawa), Vol. 2, pp. 195–202. ASME, New York (1987).
28. J. G. Georgiadis and I. Catton, Prandtl number effect on Bénard convection in porous media, *J. Heat Transfer* **108,** 284–290 (1986).
29. T. Jonsson and I. Catton, Prandtl number dependence of natural convection in porous media. In *Heat Transfer in Porous Media and Particulate Flows* (Edited by L. S. Yao, M. M. Chen, C. E. Hickox, P. G. Simpkins, L. C. Chow, M. Kaviany, P. Cheng and L. R. Davis), pp. 21–29. ASME, New York (1985).
30. V. Prasad and F. A. Kulacki, Convective heat transfer in a rectangular porous-cavity-effective aspect ratio and flow structure in heat transfer, *J. Heat Transfer* **106,** 158–165 (1984).

TRANSFERT DE MASSE PAR CONVECTION THERMIQUE A GRAND NOMBRE DE RAYLEIGH DANS UN MILIEU POREUX CHAUFFE PAR LE BAS

Résumé—On étudie à la fois théoriquement et numériquement le transfert de masse par convection de Benard à grand nombre de Rayleigh dans une couche poreuse saturée bidimensionnelle chauffée par le bas. On s'intéresse particulièrement à l'écoulement de Darcy, aux échelles des transferts de chaleur et de masse de la cellule unique (rouleau) qui existe dans le régime de convection permanente bidimensionnelle. Les solutions numériques sont basées sur les équations complètes et couvrent le domaine 50–2000 du nombre de Rayleigh. Les résultats numériques s'accordent avec les conclusions théoriques d'une analyse scalaire basée sur (i) deux échelles de température dans la cellule, (ii) un champ d'écoulement sans couches limites horizontales, et (iii) des régions terminales thermiques à la base et au sommet qui ne sont pas suffisamment minces pour être des couches limites. En désignant par Le le nombre de Lewis, le flux de transfert de masse ou le nombre de Sherwood est à l'échelle de $Le^{1/2}Ra^{7/8}$ si $Le > Ra^{1/4}$, de $Le^2 Ra^{1/2}$ si $Ra^{-1/4} < Le < Ra^{1/4}$, et de $O(1)$ si $Le < Ra^{-1/4}$. La transition entre l'écoulement de Darcy et l'écoulement de Forscheimer dominé par l'inertie est discutée ensuite avec les échelles du régime de Forschheimer.

STOFFTRANSPORT DURCH NATÜRLICHE KONVEKTION BEI HOHEN RAYLEIGH-ZAHLEN IN EINER VON UNTEN BEHEIZTEN PORÖSEN SCHICHT

Zusammenfassung—Der folgende Beitrag beschreibt eine theoretische und numerische Untersuchung des Stofftransports durch Bénard-Konvektion bei hohen Rayleigh-Zahlen in einer zweidimensionalen gesättigten porösen Schicht, die von unten beheizt wird. In dieser Untersuchung wird in erster Linie die Darcy-Strömung, der Wärme- und der Stofftransport in einer Roll-Zelle untersucht, welche sich bei der zweidimensionalen stationären Konvektion bildet. Die numerischen Lösungen werden aus dem vollständigen Gleichungssystem für zweidimensionale Strömungen gewonnen und gelten für Rayleigh-Zahlen von 50 bis 2000. Die numerischen Ergebnisse stimmen sehr gut mit den theoretischen Ergebnissen einer Ähnlichkeitsbetrachtung überein, die auf folgenden Annahmen beruht: (i) Es gibt zwei Maßstäbe für die Temperaturdifferenz in der Zelle, (ii) das Strömungsfeld hat keine waagerechten Grenzschichten und (iii) die thermischen Endbereiche oben und unten sind nicht dick genug, um Grenzschichten zu sein. Der Gesamt-Stoffübergang bzw. die Sherwood-Zahl hängen von folgenden Ausdrücken ab: $Le^{1/2}Ra^{7/8}$ für $Le > Ra^{1/4}$, $Le^2 Ra^{1/2}$ für $Ra^{-1/4} < Le < Ra^{1/4}$; Sh ist von der Größenordnung O(1) für $Le < Ra^{-1/4}$. Der Übergang von der Darcy-Strömung zu der von Massenträgheit bestimmten Forschheimer-Strömung und die Ähnlichkeitsfunktionen dieses Bereichs werden im letzten Abschnitt diskutiert.

МАССОПЕРЕНОС В НАГРЕВАЕМОЙ СНИЗУ ПОРИСТОЙ СРЕДЕ ПРИ БОЛЬШИХ ЧИСЛАХ РЭЛЕЯ

Аннотация—Проведено теоретическое и численное исследование массопереноса в режиме конвекции Бенара при больших числах Рэлея в нагреваемом снизу двумерном пористом слое. Основное внимание уделяется течению Дарси и масштабам тепло-и массопереноса в единичной ячейке (вихре), характерной для установившегося двумерного конвективного режима. Численные исследования основаны на использовании полных определяющих уравнений для двумерного потока в диапазоне изменения числа Рэлея от 50 до 2000. Численные результаты хорошо согласуются с выводами теоретического анализа, который учитывает (1) два масштаба разности температур в ячейке, (2) поле течения без горизонтальных пограничных слоев и (3) тепловые верхнюю и нижнюю концевые области, которые нельзя рассматривать как пограничные слои из-за большого поперечного размера. Обозначив число Льюиса через Le, суммарную скорость массопереноса или число Шервуда можно представить как: $Le^{1/2}$ $Ra^{7/8}$ при $Le > Ra^{1/4}$, Le^2 $Ra^{1/2}$ для $Ra^{-1/4} < Le < Ra^{1/4}$ и $O(1)$, если $Le < Ra^{-1/4}$. В заключительном разделе рассматриваются переход от течения Дарси к течению Форшхаймера, в котором преобладают силы инерции, а также масштабы режима течения Форшхаймера.